

## AUTHOR QUERY FORM

	<p>Journal: J. Chem. Phys.</p> <p>Article Number: JCP24-AR-04206</p>	<p>Please provide your responses and any corrections by annotating this PDF and uploading it to AIP's eProof website as detailed in the Welcome email.</p>
---	--	--

Dear Author,

Below are the queries associated with your article. Please answer all of these queries before sending the proof back to AIP.

**Article checklist:** In order to ensure greater accuracy, please check the following and make all necessary corrections before returning your proof.

1. Is the title of your article accurate and spelled correctly?
2. Please check affiliations including spelling, completeness, and correct linking to authors.
3. Did you remember to include acknowledgment of funding, if required, and is it accurate?

Location in article	Query/Remark: click on the Q link to navigate to the appropriate spot in the proof. There, insert your comments as a PDF annotation.
<a href="#">Q1</a>	Please check that the author names are in the proper order and spelled correctly. Also, please ensure that each author's given and surnames have been correctly identified (given names are highlighted in red and surnames appear in blue).
<a href="#">Q2</a>	In the sentence beginning "It has effect...", please confirm that "later section" refers to Sec. III B.
<a href="#">Q3</a>	Please provide volume number in Ref. 55.
<a href="#">Q4</a>	We were unable to locate a digital object identifier (doi) for Ref. 55. Please verify and correct author names and journal details (journal title, volume number, page number, and year) as needed and provide the doi. If a doi is not available, no other information is needed from you. For additional information on doi's, please select this link: <a href="http://www.doi.org/">http://www.doi.org/</a> .
<a href="#">Q5</a>	Please confirm ORCIDs are accurate. If you wish to add an ORCID for any author that does not have one, you may do so now. For more information on ORCID, see <a href="https://orcid.org/">https://orcid.org/</a> .  <a href="#">Vikki Anand Varma</a> – 0000-0002-1646-1704 <a href="#">Sujin B. Babu</a> – 0000-0002-2006-5376

Thank you for your assistance.

# Dimensional confinement and superdiffusive rotational motion of uniaxial colloids in the presence of cylindrical obstacles

Cite as: J. Chem. Phys. 162, 000000 (2025); doi: 10.1063/5.0238648

Submitted: 13 September 2024 • Accepted: 17 December 2024 •

Published Online: 9 99 9999



Vikki Anand Varma and Sujin B. Babu<sup>a)</sup>

## AFFILIATIONS

Out of Equilibrium Group, Department of Physics, Indian Institute of Technology Delhi, New Delhi 110016, India

<sup>a)</sup>Author to whom correspondence should be addressed: sujin@physics.iitd.ac.in

## ABSTRACT

In biological systems such as cells, the macromolecules, which are anisotropic particles, diffuse in a crowded medium. In the present work, we have studied the diffusion of spheroidal particles diffusing between cylindrical obstacles by varying the density of the obstacles as well as the spheroidal particles. Analytical calculation of the free energy showed that the orientational vector of a single oblate particle will be aligned perpendicular, and a prolate particle will be aligned parallel to the symmetry axis of the cylindrical obstacles in equilibrium. The nematic transition of the system with and without obstacles remained the same, but in the case of obstacles, the nematic vector of the spheroid system always remained parallel to the cylindrical axis. The component of the translational diffusion coefficient of the spheroidal particle perpendicular to the axis of the cylinder is calculated for the isotropic system, which agrees with analytical calculation. When the cylinders overlap such that the spheroidal particles can only diffuse along the direction parallel to the axis of the cylinder, we can observe dimensional confinement. This was observed by the discontinuous fall of the diffusion coefficient, when plotted against the chemical potential both for a single particle and for a finite volume fraction. The rotational diffusion coefficient quickly reached the bulk value as the distance between the obstacles increased in the isotropic phase. In the nematic phase, the rotational motion of the spheroid should be arrested. We observed that even though the entire system remained in the nematic phase, the oblate particle close to the cylinder underwent a flipping motion. The consequence is that when the rotational mean squared displacement was calculated, it showed a super-diffusive behavior even though the orientational self-correlation function never relaxed to zero, showing this to be a very local effect.

Published under an exclusive license by AIP Publishing. <https://doi.org/10.1063/5.0238648>

## I. INTRODUCTION

The role of shape anisotropy on the diffusivity of the colloids has been studied extensively. Most of these studies are performed for the bulk system, assuming that particles are suspended in a medium. However, in natural systems,<sup>1,2</sup> the diffusivity and other dynamical behaviors change due to many factors such as obstacles, finite size of the suspended particles, and confinement.<sup>3–5</sup> It is also known that the diffusivity decreases due to the crowding effect caused by the slowly moving heavy particles<sup>6</sup> and also polydispersity leads to an anomalous diffusion behavior.<sup>7</sup> In some cases, ions have been shown diffusing opposite to the applied potential due to bonding with the heavy molecules.<sup>8,9</sup> In the presence of the activity, the diffusivity of the isotropic particles has been shown to enhanced.<sup>10–12</sup>

Local diffusivity has been found to vary with the change in the width of the channel or the radius of the obstacle.<sup>13,14</sup> In addition, effective diffusivity has been found to reduce with the increase in the obstacle density.<sup>15,16</sup> Diffusivity has been shown to be affected by the presence of the effective force field, e.g., gravity.<sup>17</sup> In the passive particle system, diffusivity has been shown to decrease with the increase in obstacle concentration,<sup>18</sup> and the nature of glass transition at high densities has also been studied.<sup>19</sup> In the 2D system, the presence of obstacles leads to a sub-diffusive behavior<sup>20,21</sup> for the Brownian particle. The 2D confinement also leads to the anomalous behavior, in the presence of obstacles.<sup>22</sup> The confinement and the presence of obstacles lead to phase rich behaviors by changing the structural properties. In the presence of solute–solvent attractive interaction, colloids have been observed altering the alignment of the

56 nematic fluid.<sup>23</sup> The liquid crystals have been found aligning with  
57 the surface of the large spheres sandwiched between the two parallel surfaces,<sup>24</sup> forming a Saturn ring kind of structure. The study  
58 of such systems also opens a pathway for the application in various  
59 engineering solutions, e.g., electronics.

60 These observed effects depend upon the type of confinement,<sup>25</sup> absorption properties of the confining walls,<sup>26</sup> the surface roughness of the wall,<sup>27</sup> and drift forces.<sup>28</sup> Apart from these physical and chemical properties of fluid and confining geometry, the dynamics of colloidal particles also depend upon their shape,<sup>29</sup> especially in the active particle system.<sup>30</sup> For a 2D system, having confinement along one axis, the system has been shown to follow the behavior of a 1D system.<sup>3</sup> In these systems, anisotropic particles can behave differently than the isotropic particle system. In the presence of anisotropic particles, the role of obstacles has been paid less attention, specifically the study of the dynamics and structure while considering the interaction of the phase-rich anisotropic particles with obstacles.

34 These systems have been studied extensively by using both analytical and experimental approaches. For example, the mean first passage time<sup>31</sup> is shown to be an important parameter governing the kinetics of the system, especially for diffusion-limited cluster aggregation (DLCA) processes. As another example, the diffusivity of the polymer has been studied using blob theory,<sup>32</sup> an approximation done in terms of average particle size. In the presence of periodic obstacles, analytical relations have been derived for the diffusion coefficient considering them as point particles.<sup>33,34</sup> The effective diffusivity in the dimensional confinement for the two-dimensional system has been shown for the point particles,<sup>35</sup> where an obstacle configuration leads the particles to move within a channel. Few lattice-based models are also proposed for the study of the diffusion of particles with obstacles.<sup>36</sup> In most of the studies performed previously on a similar kind of system, the radius of the obstacles considered is much bigger than the size of the Brownian particles.<sup>37</sup> In all these studies, the shape anisotropy of the particles was not considered. In a case, where analytical approaches become very difficult to follow, simulation can be a useful tool. In simulation, different coarse-grained models provide an excellent advantage for studying comparatively complex systems. The anomalous diffusivity in the presence of crowded media has been studied in periodic obstacles where the motion becomes diffusive in the long time limit.<sup>6,38</sup>

77 In the present work, we have considered a system of anisotropic particles in the presence of the periodic arrangement of cylindrical obstacles. Depending upon the density of the obstacles, the system is effectively confined. For example, at the high density of cylindrical obstacles,<sup>28</sup> particles are constrained to diffuse in one dimension. In this way, at different obstacle configurations, we studied the structure, kinetics, and dynamics emerging in such a phase rich system of hardcore particles.

78 For highly elongated particles, the system is well known to encounter nematic alignment. In our case, the director axis has been found to align with the obstacles. In the present study, we also observed that the rotational dynamics of the oblate particles are not freezing despite being in the nematic phase. Nematic-isotropic transition lines have been found to shift in the two-component system.<sup>39</sup> In the presence of confinement, the orientation of the nematic director could be controlled as well, for example hard rods have been found to align along the plane of the substrate, shown using

114 density functional theory.<sup>40</sup> Alignment of the particles depending upon the boundary of the medium has been found to govern the crack patterns,<sup>41,42</sup> growth of bacteria,<sup>43</sup> etc. The presence of obstacles has also been found to affect the self-assembly of Brownian particles.<sup>44–46</sup> The presence of different types of particles or obstacles also alters the phase boundary, as shown in the binary mixture of hard-spheroid–sphere and sphere–rod systems.<sup>47,48</sup> However, in the presence of cylindrical obstacles, despite governing the orientation of the nematic director, the system shows no alteration in its nematic-isotropic phase boundary. These kinds of behaviors can help us design colloidal systems with robust control<sup>49</sup> over structural properties for a variety of applications.

## II. SIMULATION METHOD

126 We start the simulation by randomly distributing  $N$  number of particles in a cubic box with edge length  $L$ , where all the lengths have been considered in the unit of  $d = 1$ , the diameter of the spherical Brownian particle. Thus, the volume fraction of the particles is defined over the available volume  $V - \pi r_o^2 L$  such that  $\phi = \frac{N}{V - \pi r_o^2 L}$ , where  $V = L^3$ . The volume of the anisotropic particle with the major axis length  $a$  and minor axis length  $b$  having aspect ratio  $p = a/b$  is always kept equal to the volume of a sphere with diameter  $d = 1$ . Thus, the volume fraction of the spheroidal particles is given by  $\pi/6ab^2$ . The shape anisotropic spheroidal particle orientation vector  $\hat{n}$  has been considered along its symmetry axis. The number of particles considered is in the range of 500–2500, and  $p$  is simulated in the range 0.25–4. The cylindrical obstacles of radius  $r_o$  and length  $L$  are placed parallel to each other along the  $z$  direction on a square lattice. A periodic boundary condition is applied in the cubic box. The density of the obstacles is defined in terms of the area fraction  $\phi_o$  calculated in the plane perpendicular to the axis of cylinders, where  $\phi_o = \rho_o \pi r_o^2$  such that  $\rho_o$  is the number fraction of the obstacles defined as  $\rho_o = \frac{N_o}{L^2}$ .

132 We used the ellipsoid contact function (ECF)<sup>50</sup> to check the overlap between the spheroids. The same criterion is used to check the overlap between a cylinder and a particle. A cylinder is created by positioning spheres close enough to each other along the cylindrical axis so that the surface remains featureless.

133 To perform the dynamics of the particles, we used the Brownian-cluster-dynamics (BCD) simulation technique.<sup>51</sup> Using this method structure, kinetics and dynamics for a variety of different types of Brownian particles such as sphere<sup>52–54</sup> and spheroids<sup>55,56</sup> are studied. In this method, we randomly select particles  $2N$  times and perform either a rotational or a translational movement with equal probability. It ensures that each particle is translated or rotated at least once, in each simulation step. For the translational movement, we displace the particle in a random direction with a fixed step length  $S_T$ . Similarly, for the rotational motion, the tip of the orientation vector  $\hat{n}$  performs a 2d random walk over the surface of a sphere, with a fixed rotational step length  $S_R$ , such that  $S_T$  and  $S_R$  satisfy the following relation:

$$S_R^2 = 2S_T^2. \quad (1)$$

134 The relation between the simulation time  $t_{Sim}$  and the physical time  $t_{Phy}$  is given by  $\frac{t_{Phy}}{t_0} = t_{Sim} \frac{S_T^2}{d^2}$ ,<sup>39</sup> where  $t_0$  is the time required for a

single sphere to diffuse through a distance of its own diameter. After performing each movement step, we check the overlap condition of the hardcore particle and if the particles are overlapping, then we reject that particular movement.<sup>39</sup>

### A. Dynamics of the shape anisotropic particles

To implement the dynamics for the shape anisotropic particles, we calculate the translational displacement  $S_T$  along a direction parallel ( $s_T^{\parallel}$ ) and perpendicular ( $s_T^{\perp}$ ) to the spheroid's symmetry axis  $\hat{n}$ .<sup>39</sup>  $S_T^{\parallel}$  is given by

$$\frac{S_T^{\perp,\parallel}}{S_T} = \sqrt{\frac{d}{2bG_T^{\perp\text{or}\parallel}}}, \quad (2a)$$

$$\frac{S_R^{\epsilon}}{S_T} = \sqrt{\frac{2}{G_\theta}}, \quad (2b)$$

where  $G_T^{\perp\text{or}\parallel}$  is Perrin's friction factor for the diffusion of the particle perpendicular and parallel to  $\hat{n}$  and  $G_\theta$  is the friction factor for the rotational motion, which is calculated analytically for the stick boundary condition: for the prolate ( $p > 1$ ) case,

$$G_T^{\parallel} = \frac{4}{3} \left[ \frac{p}{(1-p^2)} + \frac{2p^2-1}{(p^2-1)^{3/2}} \ln \left( p + \sqrt{p^2-1} \right) \right]^{-1}, \quad (3a)$$

$$G_T^{\perp} = \frac{8}{3} \left[ \frac{p}{(p^2-1)} + \frac{2p^2-3}{(p^2-1)^{3/2}} \ln \left( p + \sqrt{p^2-1} \right) \right]^{-1}, \quad (3b)$$

$$G_\theta = \frac{2}{3} \frac{(p^4-1)}{p} \left[ \frac{(2p^2-1)}{\sqrt{p^2-1}} \ln \left( p + \sqrt{p^2-1} \right) - p \right]^{-1}, \quad (3c)$$

and for the oblate ( $p < 1$ ) case, we have

$$G_T^{\parallel} = \frac{4}{3} \left[ \frac{p}{(1-p^2)} + \frac{1-2p^2}{(1-p^2)^{3/2}} \arccos(p) \right]^{-1}, \quad (4a)$$

$$G_T^{\perp} = \frac{8}{3} \left[ \frac{p}{(p^2-1)} + \frac{3-2p^2}{(1-p^2)^{3/2}} \arccos(p) \right]^{-1}, \quad (4b)$$

$$G_\theta = \frac{2}{3} \frac{(p^4-1)}{p} \left[ \frac{(2p^2-1)}{\sqrt{1-p^2}} \arccos(p) - p \right]^{-1}. \quad (4c)$$

The parameter  $G$  is 1, and  $p = 1$  means that the particle is spherical.

### B. Surface energy calculation close to the obstacle-particle interface

The grand thermodynamical potential  $\Omega$  can be expressed as a functional of density  $\rho$ ,<sup>40,57</sup>

$$\Omega\{\rho(\mathbf{r}, \omega)\} = F_{id} + F_f + F_V + F_\mu, \quad (5)$$

where  $F_{id}$  is the ideal gas contribution given by

$$F_{id} = \int [\ln \Lambda^3 \rho(\mathbf{r}, \omega) - 1] \rho(\mathbf{r}, \omega) d\omega d\mathbf{r}. \quad (6)$$

The inter-particle interaction is counted in terms of  $F_f$  given by

$$F_f = \int f_2(\mathbf{r}_1, \mathbf{r}_2, \omega_1, \omega_2) \rho(\mathbf{r}_1, \omega_1) \rho(\mathbf{r}_2, \omega_2) d\omega_1 d\omega_2 d\mathbf{r}_1 d\mathbf{r}_2, \quad (7)$$

where  $f_2(\mathbf{r}_1, \mathbf{r}_2, \omega_1, \omega_2)$  is the Mayer function. This function has a value 1 for overlapping and 0 for non-overlapping conditions.  $F_\mu$  corresponds to the bulk chemical potential, given by

$$F_\mu = -\beta \mu \int \rho(\mathbf{r}, \omega) d\omega d\mathbf{r}, \quad (8)$$

where  $\mu$  is the chemical potential of the system at a particular volume fraction in the absence of obstacles.  $F_V$  is the free energy contribution in the presence of a cylinder given by

$$F_V = \int V_o(\mathbf{r}, \omega) \rho(\mathbf{r}, \omega) d\omega d\mathbf{r}. \quad (9)$$

We express  $\mathbf{r}$  in cylindrical coordinates as  $\mathbf{r} = \varrho \hat{\phi} + z \hat{z}$ . In Cartesian coordinates, it can be written as  $\mathbf{r} = \varrho \cos(\theta) \hat{i} + \varrho \sin(\theta) \hat{j} + z \hat{k}$ .

We express the potential in the presence of cylindrical obstacles as follows:

$$V_o = \begin{cases} +\infty, & \varrho < \varrho_m(\theta, \omega, r_o), \\ 0, & \varrho > \varrho_m(\theta, \omega, r_o), \end{cases} \quad (10)$$

where  $r_o$  is the radius of the cylindrical obstacles and  $\varrho_m$  is the minimum distance between the center of the obstacle and the center of mass of the Brownian particle, which depends upon the relative orientation of the particle and the cylinder body. For a particular system, since we have  $r_o$  as constant,  $V_o$  can be expressed as follows:

$$V_o = \begin{cases} +\infty, & \varrho < \varrho_m(\theta, \omega), \\ 0, & \varrho > \varrho_m(\theta, \omega). \end{cases} \quad (11)$$

We minimize  $\Omega\{\rho(\mathbf{r}, \omega)\}$  with respect to  $\rho(\mathbf{r}, \omega)$ , which leads to

$$\rho(\mathbf{r}, \omega) = \rho_b(\mathbf{r}, \omega) \exp[-V_o(\varrho, \theta, \omega)], \quad (12)$$

where  $\rho_b(\mathbf{r}, \omega)$  is the bulk properties of the Brownian particles that can be retrieved when  $V_o$  is zero,

$$\rho_b(\mathbf{r}, \omega) = \frac{1}{\Lambda} e^{\beta \mu} \times \exp \left[ \int f_2(\mathbf{r}, \mathbf{r}', \omega', \omega) \rho(\mathbf{r}, \omega) \rho(\mathbf{r}', \omega') d\mathbf{r}' d\omega' \right]. \quad (13)$$

The term that represents the bulk property can also be written as  $\rho_b(\mathbf{r}, \omega) = \rho_b f(\omega)$ <sup>57</sup> assuming a uniform distribution of the particles, where  $f(\omega) = f(\mathbf{n}_1 \cdot \hat{n})$  is the angular distribution of the particles calculated from the director of the nematic-alignment  $\mathbf{n}_1$ .  $f(\omega)$  can

be normalized with  $4\pi$  in the case of isotropic phase. To calculate the system's energy close to the obstacles, we consider the symmetry of the cylindrical obstacle along  $\hat{z}$ . Now,  $\rho$  can be expressed as  $\rho(\varrho, \theta, \omega)$ , which is given by

$$\rho(\varrho, \theta, \omega) = \rho_b f(\omega) \exp[-V_o(\varrho, \theta, \omega)]. \quad (14)$$

To calculate the surface energy per unit length along the symmetry axis of the obstacle, we take both the densities, bulk and close to the surface, and subtract the energy calculated by using Eqs. (6)–(9) and (12). The surface energy per unit length,  $\psi_l$ , is given by

$$\frac{\psi_l}{k_B T} = -\frac{S}{k_B} - \frac{\Delta\mu}{k_B T} \xi. \quad (15)$$

$$\Delta\mu = \mu - k_B T \ln(\Lambda^3 \rho_b / 4\pi), \quad (16)$$

$$\begin{aligned} \xi &= \int_{\theta=0}^{2\pi} \int_{\omega=0}^{\pi} \int_{\varrho=r_o}^{\infty} [\rho(\varrho, \theta, \omega) - \rho_b f(\omega)] d\varrho d\theta d\omega \\ &= -\frac{1}{2} \rho_b \int_{\theta=0}^{2\pi} \langle (\rho_m^2(\omega, \theta) - r_o^2) \rangle_{f(\omega)} d\theta. \end{aligned} \quad (17)$$

The other term contributing to the surface energy per unit length contains the rotational term coming from the anisotropic configuration of the particle and is given by

$$S_{rot} = \frac{1}{2} \rho_b \int_{\theta=0}^{2\pi} \langle (\rho_m^2(\omega, \theta) - r_o^2) \ln[4\pi f(\omega)] \rangle_{f(\omega)} d\theta, \quad (18)$$

where  $S$  is given by

$$S = S_{rot} + S_{tr}, \quad (19)$$

such that  $S_{tr} = S_{tr}^{id} + S_{tr}^m$ , where the ideal and inter-molecular terms can be defined as

$$S_{tr}^{id} = -\frac{1}{2} \rho_b \int_{\theta=0}^{2\pi} \langle (\rho_m^2(\omega, \theta) - r_o^2) \rangle_{f(\omega)} d\theta, \quad (20)$$

$$\begin{aligned} S_{tr}^m &= -\frac{1}{2} \left[ \int f_2(\varrho, \omega, \mathbf{r}', \omega') \rho(\varrho, \omega) \rho(\mathbf{r}', \omega') d\mathbf{r}' d\omega' d\varrho d\omega \right. \\ &\quad \left. - \rho_b^2 \int f_2(\varrho, \omega, \mathbf{r}', \omega') f(\omega) f(\omega') d\mathbf{r}' d\omega' d\varrho d\omega \right]. \end{aligned} \quad (21)$$

The average surface energy per unit area at the obstacle bulk interface can be expressed as

$$\frac{\Gamma}{k_B T} = \frac{3a}{2\pi[(3a/2 + r_o)^2 - r_o^2]} \frac{\psi_l}{k_B T}. \quad (22)$$

Here, the greater value of  $\mu$  contributes to the alignment of the particles along the cylinder's axis. In other words, for a higher  $\phi$  region, where  $\mu$  is greater, the parallel alignment is ensured. We took a value of  $\mu$  close to the isotropic–nematic interface and calculated Eqs. (16)–(18), (20), and (21), where Eq. (21) was calculated by using the Monte Carlo and curve-fitting methods, as the

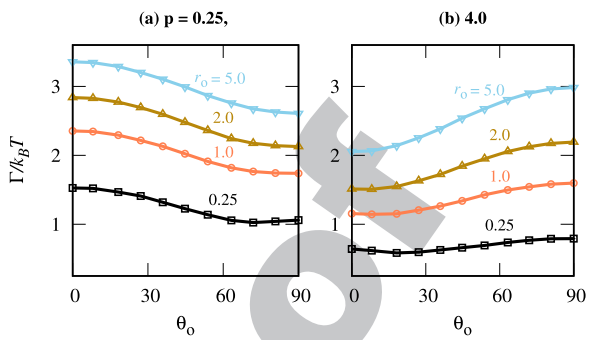


**FIG. 1.** Surface energy is calculated at different  $\theta^\circ$ , for both the oblate ( $p = 0.25$ ) and prolate ( $p = 4.0$ ) systems. Shown for the different radii of the cylindrical obstacles, as depicted in the plots. The oblate and prolate systems are energetically favored at  $\theta^\circ = 90$  and  $0$ , respectively.

function is smooth all over the region of integral. Figure 1 shows the variation in  $\Gamma/k_B T$  with the angle between the orientation of the director and the axis of the cylinder,  $\theta_o$ . For the oblate case ( $p = 0.25$ ), the angle perpendicular to the cylinder's axis is favored, over the parallel arrangement. In the case of prolate ( $p = 4.0$ ), we have a parallel alignment favored over the perpendicular alignment. The energy difference between the parallel and perpendicular alignments reduces as the radius of the obstacle  $r_o$  decreases. For thin cylinders, the energy minima occur slightly away from  $\theta_o = 90^\circ$  in the oblate and  $0^\circ$  in the prolate case. As we increase  $r_o$ , the difference between  $\Gamma/k_B T$  of minimum and maximum energy configurations increases. In other words, the control of the nematic axis is enhanced with the increase in the radius of the cylinder<sup>58</sup> at a constant number density of the obstacles.

### III. RESULTS

#### A. Kinetics of the evolution of nematic-alignment in the presence of cylindrical obstacles

Figure 1 shows the surface energy per unit volume close to the cylinder–bulk interface as given by Eq. (22), where we considered only the hardcore repulsion interaction between the cylinder and ellipsoid and between ellipsoid and ellipsoid. In addition, we have considered only a single cylindrical obstacle. In Fig. 1(a), we observe that the surface energy is minimum when the symmetry axis of the oblate particle ( $p = 0.25$ ) is perpendicular to the cylindrical axis. For the prolate particle ( $p = 4.0$ ), we observe that minimum surface energy configuration happens when the symmetry axis of the particle is parallel to the cylindrical axis. Thus, it seems that the presence of an obstacle will assist in the nematic transition for anisotropic particles.

We did not observe any significant effect on the nematic–isotropic phase line for the system where the distance between the obstacles is large enough for the particles to rotate freely. However, in the presence of obstacles at high densities, a large fraction of spheroids close to the wall remain aligned along the wall in comparison with the small fraction of particles present in the bulk isotropic regions, contributing to the high nematic order-parameter value. In all such cases, where the distance between the obstacles becomes comparable to the size of the particles, S

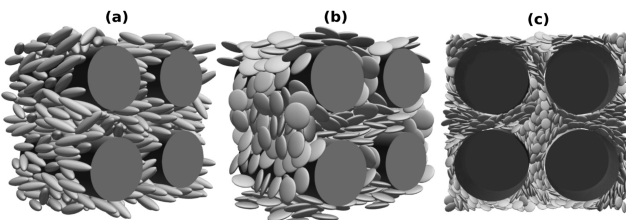


**FIG. 2.** Snapshot of the system in nematic-phase, shown at  $\phi = 0.45$  for (a)  $p = 4.0$ ,  $r_o = 2.0$ , and  $\phi_o = 0.4$ ; (b)  $p = 0.25$ ,  $r_o = 2.0$ , and  $\phi_o = 0.4$ ; and (c)  $p = 0.25$ ,  $r_o = 5.0$ , and  $\phi_o = 0.55$ , where all the three systems are in nematic phase.

remains high (e.g.,  $S = 0.65$  for  $p = 4$ ,  $\phi = 0.38$  at  $\phi_o = 0.5$ ), which agrees with the previous observations.<sup>59</sup>

We initiate the system by putting the spheroids in an energetically less favorable state as obtained from the obstacle–bulk surface energy calculation (see Fig. 1). For the oblate particle, nematic director is less favored along the symmetry axis of the cylinders, and for the prolate case, it is less favored along the perpendicular plane of the symmetry axis of the obstacles. Thus, the ellipsoids in the initial configuration are already in the nematic phase. Relaxation of the angle between the symmetry axis of the ellipsoid and the cylindrical axis for  $\phi = 0.5$ ,  $\rho_o = 0.005$ , and  $r_o = 2.0$  can be observed in Fig. 3(a). It seems that the rotational kinetics of the symmetry axis of the ellipsoids relaxes slowly up to a time of 200, and then, suddenly all the ellipsoids rearrange to the minimum surface energy configuration [see Figs. 2(a) and 2(b)] obtained from a single ellipsoidal calculation. Also note that in the absence of obstacles at  $\phi = 0.5$ , the equilibrium configuration of the ellipsoids is a nematic phase. Figure 3(b) shows the evolution of the nematic phase order parameter  $S$ , which is the largest eigenvalue of the tensor  $Q$ , defined by

$$Q_{\alpha,\beta} = \frac{3}{2} \frac{1}{N} \sum_i \langle (n_\alpha)_i (n_\beta)_i \rangle - \frac{1}{2} \delta_{\alpha,\beta}, \quad (23)$$

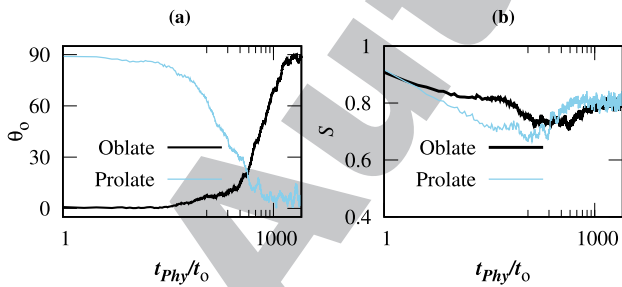


**FIG. 3.** (a) Evolution of the director of oblate and prolate systems is shown for  $r_o = 2.0$  and a low  $\phi_o = 0.063$ , at  $\phi = 0.5$ . The system starts initially from an unfavored condition for prolate ( $p = 4.0$ ) at  $\theta_o = 90^\circ$  and oblate ( $p = 0.25$ ) at  $\theta_o = 0^\circ$ , where  $\theta_o$  is the angle between the nematic director and the axis of the cylindrical obstacles. (b) The evolution of the order parameter is shown for both the oblate and prolate systems. Both the systems show stability after a long time limit ( $t_{phys} > 1000$ ).

where  $n_\alpha$  and  $n_\beta$  are the components of the particle's orientation vector ( $\hat{n}$ ) with  $\alpha, \beta \in x, y, z$ .

As the system moves toward the equilibrium state, the  $S$  parameter falls at initial times but remains well above the value 0.3, showing that the system never passes through the isotropic phase. In other words, the system remains in the nematic phase throughout the evolution in both prolate and oblate cases. The fall in the  $S$  parameter indicates the gradual change in the orientation of the particles, which is initiated from the cylinder–bulk interface and expands toward the bulk region of the ellipsoidal particles. This shows that we can make an ellipsoid particle system undergo a transition from an unfavorable nematic phase to a favorable nematic phase due to the presence of the cylindrical obstacle.

Figure 4 shows the kinetics of the evolution of  $\theta_o$  for both oblate and prolate cases in the presence of obstacles. In the case of constant  $\rho_o = 0.005$ , the kinetics of the system is higher for the system with cylinders having a greater radius, as shown in Figs. 4(a) and 4(b). A system with  $r_o = 5$  evolves faster than a system with  $r_o = 2$ . It can be explained by considering the effect of  $\phi_o = \rho_o \pi r_o^2$  such that  $\phi_o$  increases with the increase in  $r_o$ . A system with a higher

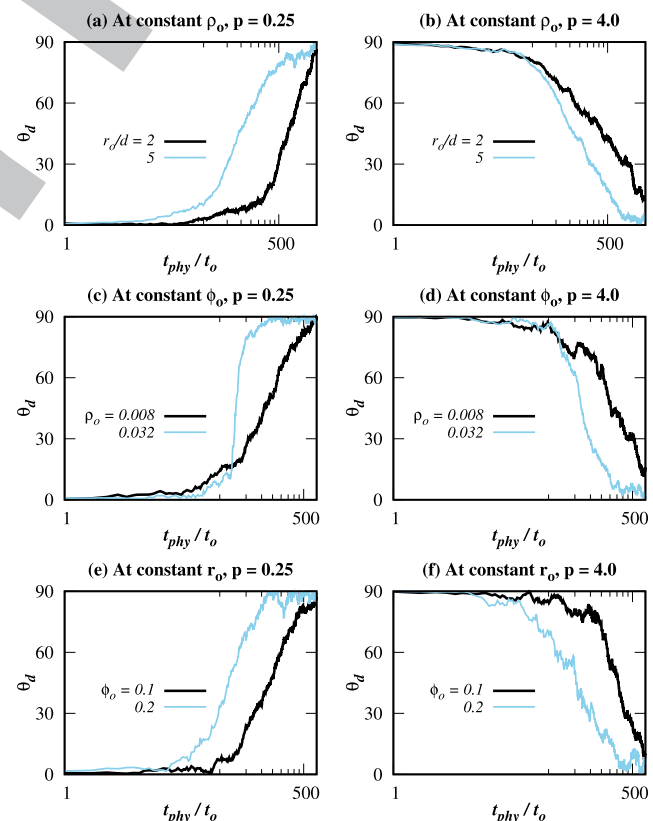


**FIG. 4.** Evolution of the directors shown at a different configuration for both the oblate and prolate systems. (a) Prolate and (b) oblate are shown at  $\phi = 0.5$  for different  $r_o/d$ , at constant  $\rho_o = 0.005$ . (c) and (d) Evolution of the oblate and prolate systems for different  $\rho_o$  and at constant  $\phi_o = 0.1$ . (d) and (f) System's evolution for different  $\phi_o$ , at constant  $r_o = 2.0$ .

surface of the obstacles will have a higher total surface energy difference between favorable and unfavorable states, which results in a faster evolution toward the favorable state. Apart from that,  $\Delta\Gamma_m$  has a higher value for the obstacles having a greater  $r_o$ ; this effect is not as dominating as the effect of obstacles–bulk interface interaction. In Figs. 4(c) and 4(d), where both the systems were simulated at constant  $\phi_o = 0.1$ , it has been shown that the system with higher  $\rho_o = 0.032$  shows a faster evolution to the favorable state.

At constant  $\phi_o$ , reducing the radius of the cylinders will increase the surface area as the number of cylinders increases in the system. In other words, the sky-blue line representing a system with  $r_o = 1.0$  has a surface area of the obstacles two times greater than the system with  $r_o = 2.0$ , at constant  $\phi_o$ . Therefore, despite having  $\Delta\Gamma_m$  higher, the system with  $r_o = 2$  shows a slower evolution than the system with  $r_o = 1$ . Similar observations are shown in Figs. 4(e) and 4(f) for the oblate and prolate systems, respectively. For the same  $r_o$ , the system with higher  $\phi_o$  has a greater surface area in contact with the ellipsoids, and therefore, the system with higher  $\phi_o$  evolves faster.

To show the structural properties of the nematic phase, we calculated the radial distribution function  $g(r)$ , as shown in Fig. 5. For  $r_o = 5$  and  $\rho_o = 0.005$ , we have the  $g(r)$  curve deviating from the usual  $g(r) = 1$  (solid line), due to the absence of particles in the obstacle regions, for both oblate and prolate cases, which is shown in Figs. 5(a) and 5(b), respectively. The dotted line represents the system with spherical particles simulated at the same configuration. However, the peaks of the curves are similar to the bulk system, where again the deviation represents a large inaccessible region for the diffusing particles. The black lines represent the system with

$r_o = 2$  simulated at the same  $\rho_o = 0.005$ , which show characteristics similar to the bulk phase, where we have a small inaccessible region in comparison with  $r_o = 5$ . For both systems, the local structure remains similar to the bulk phase. Figures 5(c) and 5(d) represent the system of oblate and prolate particles, respectively, simulated at constant  $\phi_o = 0.1$  for different obstacle radii, where the sky-blue lines represent  $r_o = 1$  and the black lines represent  $r_o = 2$ . The system, again, can be observed to be similar to the bulk phase. Figures 5(e) and 5(f) show  $g(r)$  for the system of oblate and prolate particles, respectively, simulated at constant  $r_o = 2$  for different obstacle densities, where the sky-blue lines represent  $\phi_o = 0.2$  and the black lines represent  $\phi_o = 0.1$ .

To understand the alignment of the particles in the nematic phase, we have shown  $g(\theta)$  as a function of the angle  $\theta$ , where  $g(\theta)$  is the distribution of the angle  $\theta$ , formed between  $\hat{n}$  of any two particles. For a perfectly aligned nematic system, it will show sharp peaks at  $\theta = 0^\circ$  and  $180^\circ$ . Figures 6(a) and 6(b) show the distribution  $g(\theta)$  for prolate and oblate particles, respectively, at constant  $\rho_o = 0.005$  at two different obstacle radii  $r_o = 2$  and  $r_o = 5$ .

In the case, the particles' orientation remains perpendicular to the direction of cylindrical axis, causing misalignment, which can be observed in the  $G(\theta)$  distribution [Fig. 6(a)]. It has an effect on the dynamics of the system, where it shows an anomalous rotational behavior, which has been discussed in Sec. III B. Prolate particles align with its orientation parallel to the direction of the cylindrical axis, which enhances the particles' alignment [Fig. 6(b)]. Figures 6(c) and 6(d) show the alignment calculated for the same  $\phi_o$ , where we observe that increasing the number density while decreasing the radius of the cylinders leads to better alignment in the case

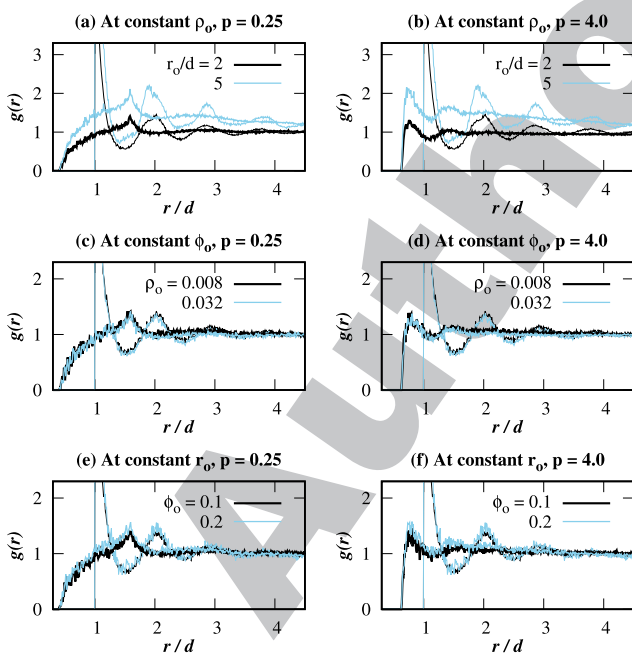


FIG. 5.  $g(r)$  is shown for the system in the nematic phase for both prolate and oblate particles: (a) and (b) at constant  $\rho_o = 0.005$ , (c) and (d) at constant  $\phi_o = 0.1$ , and (e) and (f) at constant  $r_o = 2.0$ . The thin lines represent the system of spheres equilibrated at the same configuration.

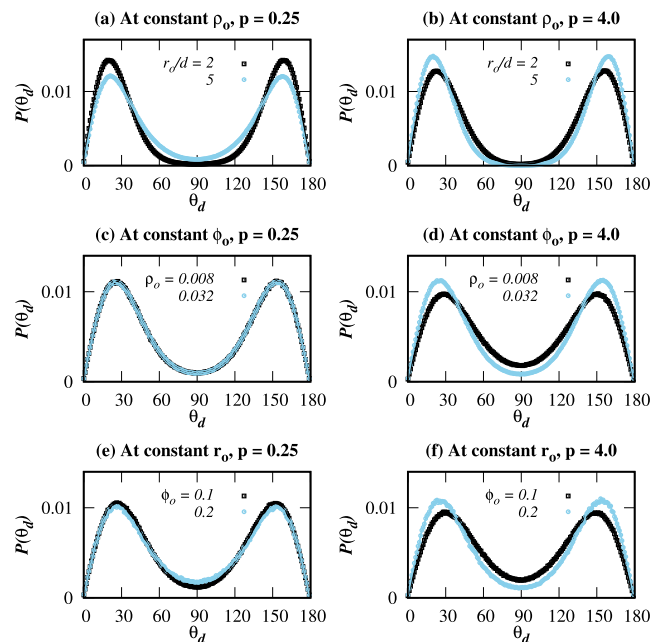


FIG. 6.  $g(\theta)$  is shown for the system in the nematic phase for both prolate and oblate particles: (a) and (b) at constant  $\rho_o = 0.005$ , (c) and (d) at constant  $\phi_o = 0.1$ , and (e) and (f) at constant  $r_o = 2.0$ .

429 of prolate particles, while for the case of oblate particles, it remains  
 430 nearly the same. With increasing  $\phi_o$ , we observed a small decrease  
 431 in alignment for the oblate particles [see Fig. 6(e)], whereas prolate  
 432 shows better alignment [see Fig. 6(f)]. In all three cases, the behavior  
 433 of oblate has been seen to be opposite to the prolate case.

## 434 B. Dynamics of the system in the presence 435 of obstacles

436 The translational diffusion dynamics of a tracer spherical particle  
 437 in crowded media depends only upon the accessible volume.<sup>60</sup>  
 438 The accessible volume is defined as the volume accessible to the center  
 439 of mass of a tracer particle. That means as we increase the volume  
 440 fraction, the diffusivity decreases and becomes dependent upon the  
 441 packing fraction.<sup>39,61</sup> Here, we are exploring the dynamics of the  
 442 ellipsoidal particle far away from the nematic transition. We also did  
 443 not take into account the hydrodynamic effect. When we assume  
 444 that the fluid particles are very small in size compared to the size  
 445 of the obstacles, the effect of hydrodynamics on the system remains  
 446 minimal.<sup>62,63</sup> We have also considered the surface of the obstacles to be  
 447 smooth and featureless.<sup>28</sup>

448 The two-dimensional diffusivity of the diffusing point particles  
 449 has been calculated analytically, in the presence of periodically  
 450 arranged immobile disks.<sup>37</sup> In order to compare with the analytical  
 451 results for finite size and shape of the diffusing particles, we considered  
 452 the obstacle configuration in terms of the trap size given as  $q$   
 453 having a trap opening width of  $w$ , as shown in Fig. 7(b).<sup>64</sup> Here,  $q$   
 454 and  $w$  can be expressed in terms of obstacle radius ( $r_o$ ) and lattice  
 455 density ( $\rho_o$ ),

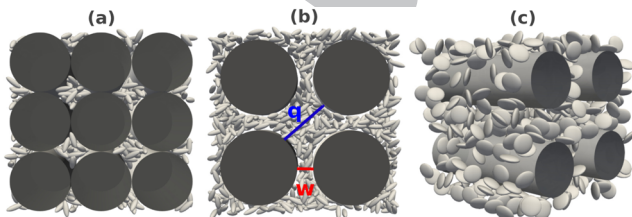
$$456 w = \sqrt{\frac{1}{\rho_o}} - 2r_o, \quad (24a)$$

$$457 q = \sqrt{\frac{2}{\rho_o}} - 2r_o. \quad (24b)$$

458 The effective translational diffusivity of the point particles in the  
 459 presence of the 2d array of the obstacles is given by<sup>37</sup>

$$460 D_T^{eff} = \frac{1}{\langle w'(x) \rangle \langle 1/w'(x) D(x) \rangle}, \quad (25)$$

461 where  $w(x)$  is the channel's width, which changes with positions.  
 462  $w'(x)$  is the derivative of the channel width with respect to position.<sup>37</sup>  $D(x)$  is the position dependent diffusivity.  
 463



464 **FIG. 7.** Snapshot of the isotropic system shown at particle concentration  
 465  $\phi = 0.2$  for different obstacle configurations: (a)  $q = 3.0$ ,  $w = 0.0$ , and  $r_o = 3.6$ ;  
 466 (b)  $q = 7.0$ ,  $w = 2.0$ , and  $r_o = 5.0$ ; and (c)  $q = 2.3$ ,  $w = 2.0$ , and  $r_o = 2$ , where  
 467  $w$  and  $q$  are the lengths measured in units of  $d_o$ , as shown in panel (b).

We consider the diffusion coefficient to be a constant (independent of the position) and equal to  $D_2^P$  (maximum possible diffusivity for a given obstacles' lattice configuration) and solve Eq. (25). The analytical expression for the effective diffusivity due to Fick–Jacob  $D_T^{FJ}$  is then given by<sup>37</sup>

$$473 D_T^{FJ} = \frac{1}{D_2^P} \left( \frac{2}{\sqrt{1-f_w^2}} - \arctan \left( \frac{\sqrt{1+f_w}}{1-f_w} \right) - \frac{\pi}{2} + 1 - f_w \right). \quad (26)$$

However, this assumption is not accurate as in the presence of obstacles, the volume accessible to the ellipsoidal particles to diffuse will depend on the width of the channel formed between the obstacles. Thus, the diffusivity of the ellipsoids  $D_T(x)$  will be position dependent.

Reguera and Rubi<sup>65</sup> considered the short time diffusion of the point particles to be position dependent such that  $D_T(x) = D_2^P/[1+w'(x)/4]^{1/3}$ . The effective diffusivity  $D_T^{RR}$  is given by

$$483 D_T^{RR} = \frac{1}{\left(1 - \frac{\pi}{4}f_w^2\right)} \times \frac{1}{\left[f_w \int_0^{\pi/2} \frac{(\cos \phi)^{1/3} d\phi}{(1-f_w \cos \phi)} + 1 - f_w\right]}, \quad (27)$$

where  $f_w$  is given as  $(\sqrt{1/\rho_o} - w)/(\sqrt{1/\rho_o} - d_p)$  with  $\sqrt{1/\rho_o}$  being the lattice constant for the obstacle configuration and  $d_p$  being the length of the minor axis. At  $f_w = 0$ , we have infinitely thin cylinders and the channel opening  $w$  between the cylinders reaches its maximum value, which is equal to the lattice constant  $\sqrt{1/\rho_o}$ . At  $f_w = 1$ , the channel width is so small that ( $w = d_p$ ) no ellipsoidal particle can escape; thus, the diffusivity perpendicular to the cylindrical axis goes to zero. To compare the diffusivity of a particle with a finite volume with that of the point particle model, we have kept  $q$  the trap size constant while changing  $f_w$ . In other words, both the lattice constant and the radius of the obstacles are varied to maintain the desired trap size  $q$  and channel width  $w$ , which are the relevant parameters governing the diffusivity of the ellipsoidal particles.

We calculated the long-time diffusivity of the spheroids in the plane perpendicular to the axis of the cylinder by changing  $f_w$  at different constant  $q$  values as shown in Fig. 8. The resulting two-dimensional translational diffusivity  $D_T^2$  for the single particle at  $f_w = 0$  for a particular trap size  $q$ .  $D_T^2$  for spheres [Fig. 8(a)] agrees with  $D_T^{RR}$  (green solid line); however,  $D_T^{FJ}$  overestimates the diffusivity of the ellipsoidal particles. When we increase the anisotropy of the ellipsoidal particle by changing  $p$ , we observe significant deviation from the analytical calculation; see Figs. 8(b)–8(d). For the prolate particles, the deviation from the analytical calculation happens when  $f_w > 0.5$  as can be observed in Figs. 8(b) and 8(c). It can also be observed that when the trap size  $q$  is smaller, the deviation from analytical calculation happens at lower  $f_w$ . For the disk like particles [Fig. 8(d)], the deviation from the analytic calculation happens at a smaller  $f_w$  than for the needle like particles. Also note that in the absence of obstacles, both the system  $p = 0.333$  and 3.0 show almost the same diffusivity.<sup>39</sup>

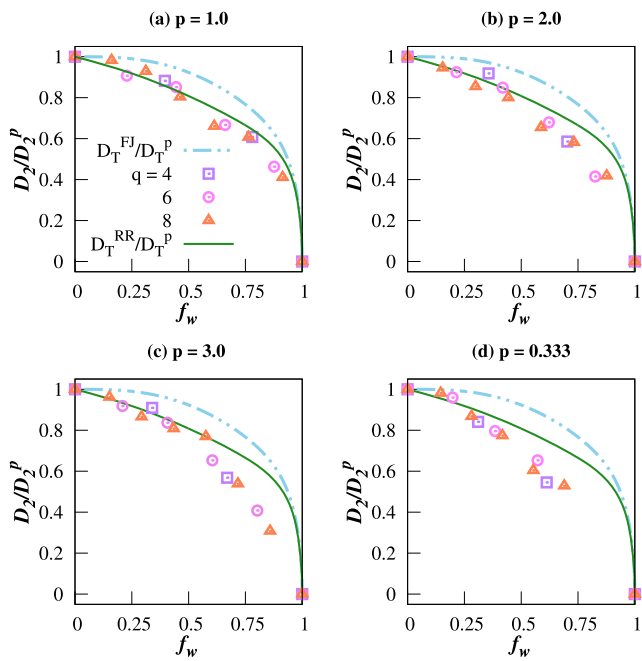


**FIG. 8.** Variation in 2D translational diffusivity  $D_2/D_2^p$  of a single spheroid shown at different cage openings  $f_w$ , measured in the laboratory frame in the plane perpendicular to the cylindrical axis, for  $w = 4$  (square), 6 (circle), and 8 (triangle). (a) For spheroids with  $p = 1.0$ , (b) 2.0, (c) 3.0 (rod like particles), and (d) 0.333 (disk like particles). All the diffusivities have been normalized by  $D_2^p$ , the diffusivity at  $f_w = 0$  (for the constant radius of obstacles  $\rho_o = 0$ ).

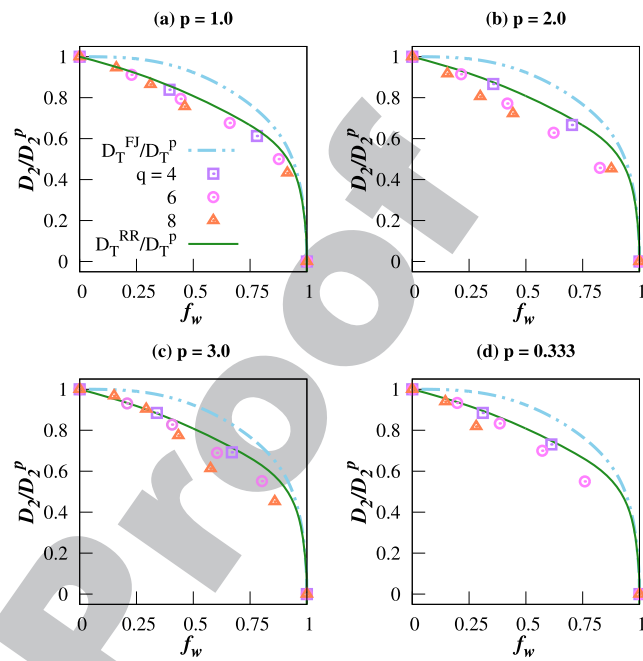


**FIG. 9.** Variation in 2D translational diffusivity  $D_2/D_2^p$  of spheroids at a finite concentration ( $\phi = 0.2$ ), shown at different cage openings  $f_w$ , for  $w = 4$  (square), 6 (circle), and 8 (triangle). (a) For spheroids with  $p = 1.0$ , (b) 2.0, (c) 3.0, and (d) 0.333.

516  
517  
518  
519  
520  
521

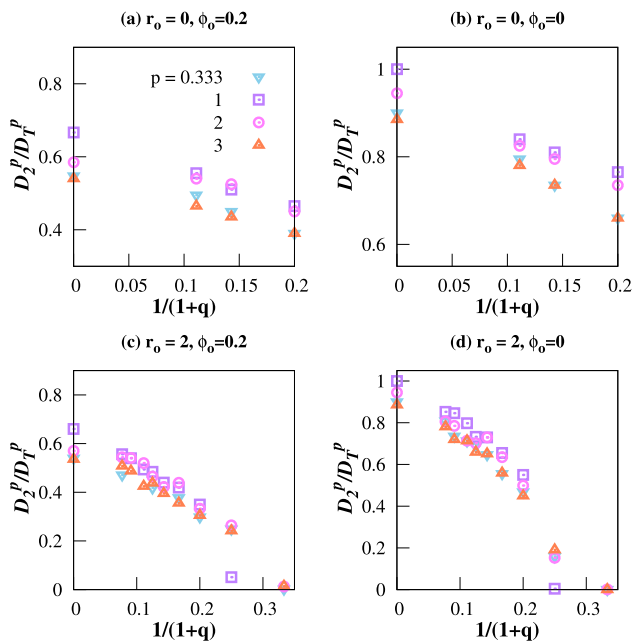
To compare with the expression of the diffusivity given for the point particles, we calculated  $D_2$  and normalized with  $D_2^p$ , which is the maximum  $D_2$  possible at a constant  $q$  (at  $f_w = 0$ ) for a given finite volume fraction  $\phi = 0.2$ . For the spherical particles, the diffusivity follows the analytical curve as in the case of single particle diffusivity as shown in Fig. 9(a). However, for the ellipsoidal particles also, we have less deviation from the analytical curve in comparison with the single particle diffusivity, as shown in Figs. 9(b)–9(d) calculated for  $p = 2.0$ , 3.0, and 0.333, respectively. It indicates that for the particles at a finite volume fraction in the isotropic phase, the caging effect due to the obstacles remains the same regardless of the shape of the particle.

For a particular constant  $q$  value, the diffusivity will be maximum  $D_2^p$  at  $f_w = 0.0$  (at constant  $r_o = 0$ ). Figure 10 shows variation in  $D_2^p$  with  $q$ , where the x-axis is scaled as  $1/1 + q$ , which varies between 0 and 1, as  $q$  varies between  $\infty$  and 0.  $q = \infty$  represents a system without obstacles. In the larger trap size regions, the diffusivity varies almost linearly regardless of their shapes [Figs. 10(a) and 10(b)]. One difference between the Lorentz gas model and the finite size particle is that  $D_2^p$  of the Lorentz gas model would be maximum and same at all the  $q$  values<sup>64</sup> for  $f_w = 0$ . To find out the variation in  $D_2^p$  in the small trap size regions (comparable with the particle's size), we calculated diffusivity at  $r_o = 2.0$  [Fig. 10(c)] shows  $D_2^p$  at a finite concentration and Fig. 10(d) for single particles]. For the spherical particles (square points), diffusivity drops abruptly. However, the drop in the diffusivity of the anisotropic particles remains linear almost throughout the whole  $q$  regions.

The dynamics of the ellipsoidal particle is related to the volume accessible to the center of mass of the ellipsoidal particles also known as accessible volume, due to the finite size of the obstacles and the ellipsoids. If the accessible volume is small, it will lead to caging and dimensional confinement. The diffusivity of the ellipsoidal particles goes to zero when the channel width is close to the ellipsoidal particle's size. The accessible volume is related to the chemical potential of the hard sphere particle system<sup>66</sup> given by  $\mu/k_B T = -\ln \frac{\phi_a}{\phi}$ , where  $\mu$  is the chemical potential of the hard sphere particles at volume fraction  $\phi$  and having an accessible volume  $\phi_a$ . In Fig. 11, we have plotted the chemical potential calculated using Widom's particle insertion method for different  $\phi$  with varying  $w/d_o$  and  $q/d_o$  at different  $\phi_o$ . For constant  $w/d_o$  values,  $\mu/k_B T$  decreases with an increase in  $q/d_o$  and becomes constant in the large  $q/d_o$  regime corresponding to a large accessible volume. When  $w < d_o$  and  $q < d_o$ ,  $\mu/k_B T$  increases and it becomes increasingly difficult to access the free volume for the ellipsoidal particle. A higher  $\mu/k_B T$  represents a lower accessible volume, which leads to a decrease in the diffusivity of the particles.

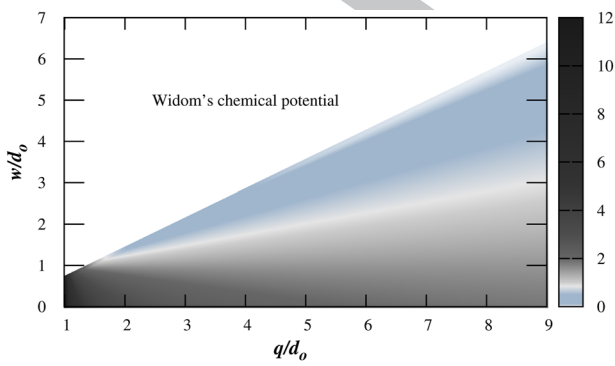
Experimentally, the diffusivity of the tracer particles has been shown to fall exponentially with the increase in the concentration of heavy globular proteins in the aqueous solution,<sup>2</sup> due to the decrease in the accessible volume for the tracer particle. To show the effect of the confinement and excluded volume,  $\phi$  and  $\phi_a$ , on the translational diffusivity, we have shown  $D_T/D_T^p$  as a function of Widom's chemical potential  $\mu/k_B T$  for the spherical [p = 1.0 Fig. 12(a)] and spheroidal particles [prolate, p = 2.0 Fig. 12(b)]. At this  $p$ , we will

549  
550  
551  
552  
553  
554  
555  
556  
557  
558  
559  
560  
561  
562  
563  
564  
565  
566  
567  
568  
569  
570  
571  
572  
573  
574  
575  
576  
577  
578

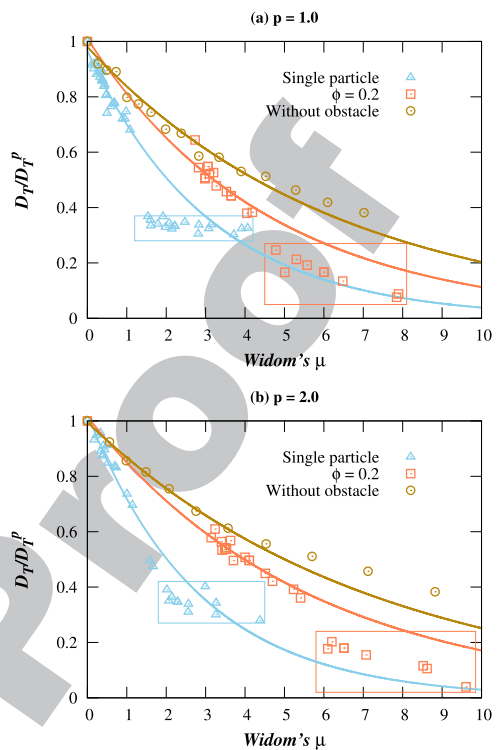


579  
580 FIG. 10. Variation in  $D_2^p/D_T^p$  with  $1/(1+q)$ , where  $D_2^p$  is the diffusivity shown  
581 for the cylinders with a constant and infinitely thin radius ( $r_0 = 0$ ). (a) At finite  
582 particle's concentration and (b) at infinitely dilute concentration. Variation in  $D_2^p$  also  
583 shown for the finite radius ( $r_0 = 2$ ) (c) at finite particle's concentration and (d) at  
584 infinitely dilute concentration, where all the diffusivity values have been scaled by  
 $D_T^p$ , the diffusivity of single spheroids in the bulk phase.

585 always have an isotropic fluid phase irrespective of  $\phi$ . The diffusivity  
586 of the system with respect to  $\mu/k_B T$  is shown at a finite spheroid  
587 concentration and infinite spheroid dilution (single particle) in  
588 comparison with the diffusivity of hard spheroids at different  $\phi$  without  
589 the presence of obstacles. We can observe that a sudden sharp fall  
590 in the diffusivity of the spherical particle and prolate particle as  
591  $w/d_o$  falls below 1.0 (size of the particle) as shown in Figs. 12(a)  
592 and 12(b), respectively. Interestingly, in the case of single particle,



593 FIG. 11. Widom's chemical potential is shown by the colored map in the  $q-w$  plane.

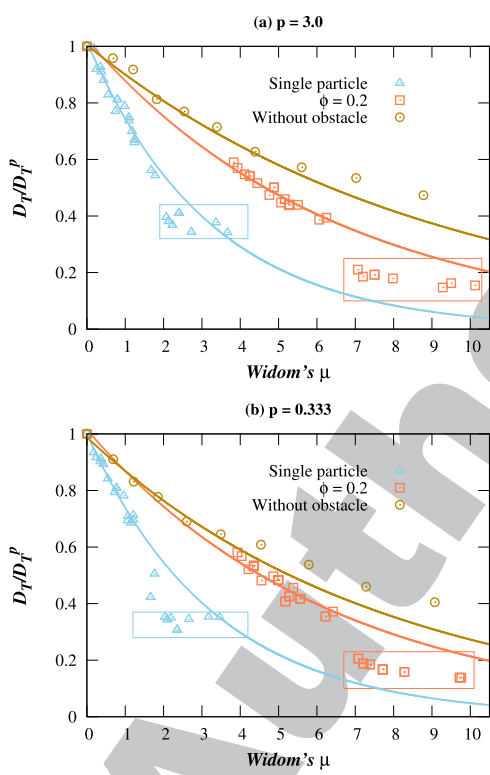


594 FIG. 12. Translational diffusivity  $D_T/D_T^p$  normalized by the diffusivity of the particle  
595 in infinite dilution  $D_T^p$  is shown as a function of Widom's chemical potential for  
596 (a) spherical particles and (b) prolate particles. The blue triangles represent  
597 the single particle diffusivity within the presence of obstacles. The coral squares  
598 represent the diffusivity at a finite particle concentration with  $\phi = 0.2$ , compared  
599 with the diffusivity at different particle concentrations  $\phi$  in the absence of obstacles  
600 represented by dark-golden circles. The solid lines represent the exponential fits.  
601 The points inside the rectangular bracket represent the system with 2d confinement  
602 ( $s < 1.0$ ), where the particles can only move in the 1d pore confined by the  
603 cylindrical obstacles.

604 the diffusion coefficient becomes independent of the obstacle  
605 concentration for both spherical and prolate particles. The reason is  
606 that the sphere and the prolate particle can only diffuse along one  
607 dimension, which is parallel to the axis of the cylinder. The diffusion  
608 coefficient  $D_T/D_T^p$  for a spherical and the prolate particle along one  
609 dimension in simulations is  $\sim 0.35$ , which is the approximate value  
610 we observe for spheres. At a finite concentration ( $\phi = 0.2$ ), the dif-  
611 fusivity keeps decreasing with increasing  $\mu/k_B T$  due to the increase  
612 in  $\phi$ , as the effective accessible volume fraction decreases due to the  
613 excluded volume between the two ellipsoidal particles. Also with the  
614 increase in the radius of the cylindrical obstacle, all the ellipsoidal  
615 particles may get aligned in a column.<sup>3</sup> This is the minimum energy  
616 configuration for a single prolate particle in the presence of the cyl-  
617 inical obstacle. Thus, for a finite volume fraction, once the ellipsoids  
618 are aligned, then the diffusion is only possible along one dimension,  
619 which is along the direction of the cylindrical axis. We observe that  
620 the diffusivity of the ellipsoidal particle at  $\phi = 0.2$  [Figs. 12(a) and  
621 12(b)] follows the fitted exponential curve, which falls suddenly to  
622 a lower value. This is again due to the one-dimensional confinement

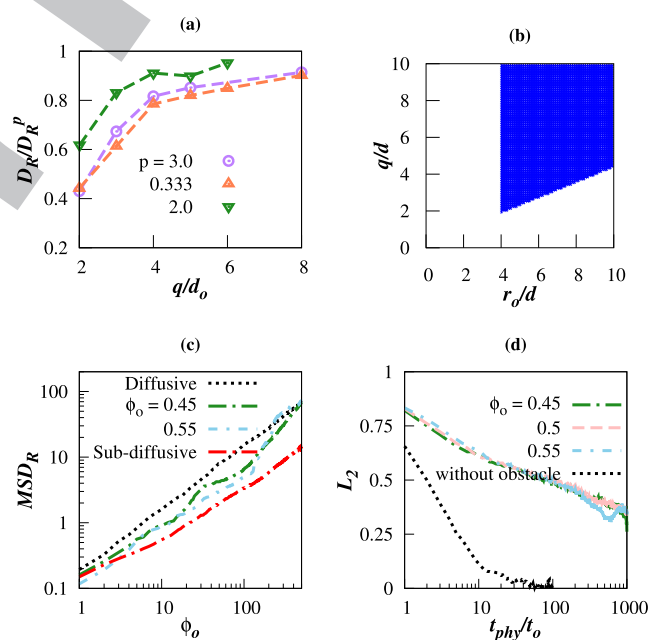
623 of the ellipsoidal particle. Compared to the single particle diffusion,  
 624 which was a constant after confinement along one dimension for  
 625  $\phi = 0.2$  even after confinement, the diffusion coefficient falls due to  
 626 the finite volume fraction of the ellipsoids. In all the cases, the diffusivity  
 627 in the presence of obstacles remains lower than the diffusivity  
 628 in the spherical particle at finite  $\phi$  without the obstacle.

629 To show the effect on the dynamics of highly anisotropic particles,  
 630 we took oblate and prolate particles with  $p = 3.0$  and  $p = 0.333$ ,  
 631 respectively. It should be noted that the presence of cylindrical obstacles  
 632 does not change the isotropic–nematic boundary in the  $\phi$ - $p$   
 633 plane. Figures 13(a) and 13(b) show the variation in  $D_T/D_T^p$  of both  
 634 prolate and oblate particles, respectively, as a function of  $\mu$ , calcu-  
 635 lated at  $\phi = 0.2$ . At this  $\phi$ , the systems corresponding to both prolate  
 636 and oblate remain isotropic for all the points shown in Figs. 13(a)  
 637 and 13(b). The translational diffusivity behaves in the same way as  
 638 a spherical particle system. The ellipsoidal system still shows a sud-  
 639 den drop with  $\mu$  as the diffusivity perpendicular to the cylinder axis  
 640 drops to zero as discussed earlier for the spherical system.



641 **FIG. 13.** Translational diffusivity  $D_T/D_T^p$  normalized by the diffusivity of the particles  
 642 in infinite dilution  $D_T^p$  is shown as a function of Widom's chemical potential for highly  
 643 anisotropic particles: (a) prolate ( $p = 3.0$ ) and (b) oblate ( $p = 0.333$ ). The blue  
 644 triangles represent the single particle diffusivity within the presence of obstacles.  
 645 The coral squares represent the diffusivity at a finite particle concentration  $\phi$  in the  
 646 absence of obstacles represented by dark-golden circles. The solid lines represent  
 647 the exponential fits. The points inside the rectangular bracket represent the system  
 648 with  $2d$  confinement ( $s < 1.0$ ), where the particles can only move in the  $1d$  pour  
 649 confined by the cylindrical obstacles.

651 Unlike the translational diffusivity, which depends dominantly  
 652 on the channel width  $w/d_o$ , the rotational diffusivity is found to  
 653 depend dominantly on the trap size  $q/d_o$ . At a large  $q/d_o$ , the rota-  
 654 tional diffusivity remains decoupled with the translational diffusivity  
 655 in the isotropic phase. Figure 14(a) shows the variation in rotational  
 656 diffusivity  $D_R/D_R^p$  with  $q/d_o$ .  $D_R/D_R^p$  is shown to stagnate quickly  
 657 with the increase in  $q/d_o$  reaching the diffusion coefficient of the  
 658 bulk system in the absence of obstacles ( $D_R^p \sim 0.33, 0.56, 0.66$ , for  
 659  $p = 3.0, 0.33, 2.0$ , respectively, calculated at  $\phi = 0.2$ ) for both prolate  
 660 and oblate systems. However, in the nematic phase, the disk like  
 661 particles show strong coupling between translational and rotational  
 662 diffusivities. In the absence of obstacles, the rotational motion in the  
 663 nematic phase shows a sub-diffusive behavior in the long time limit.  
 664 However, in the presence of obstacles with high  $r_o/d > 4$ ,  $D_R/D_R^p$  of  
 665 the oblate particles present in the nematic phase near the obstacle's  
 666 comes out of the dynamic arrest configuration. As it has been shown  
 667 in the  $g(\theta)$  calculation [Fig. 6(a)], with a higher radius, the obsta-  
 668 cle structure gets frustrated locally, providing space for the flipping  
 669 of the particle. The region over which we observe the anomalous  
 670 behavior is shown as the shaded region in Fig. 14(b) in the  $q/d - r_o/d$   
 671 plane, where the disk like particles with  $p = 0.25$  were considered.



672 **FIG. 14.** (a) Rotational diffusivity  $D_R/D_R^p$  is shown with the change in obsta-  
 673 cle configuration, for  $p = 3.0$  (circles),  $p = 0.333$  (upper triangle), and  $p = 2.0$   
 674 (lower triangle), at particle concentration  $\phi = 0.2$ . (b) Blue region shown in the  
 675  $q-r_o$  plane represents the configuration of obstacles, where the disk like particles  
 676 show a diffusive behavior at long time scale despite being in nematic phase (for  
 677  $\phi_o > 0.425$ ). (c)  $MSD_R$  is shown for the oblate particles ( $p = 0.25$ ) flipping at  
 678 ( $\phi = 0.45$ ), for different obstacle concentrations  $\phi_o$ , for a large obstacle size  
 679  $r_o = 5.0$ . The red line shows  $MSD_R$  averaged over all the particles. The black line  
 680 is a guide to the perfectly diffusive behavior. (d) Decay of  $L_2$  with time is shown.  
 681 Long dashed lines represent the different  $\phi_o$  as given in the legend, compared  
 682 with the decay of  $L_2$  for  $D_R/D_R^p = 0.2$  in the absence of obstacles calculated at  
 683  $\phi = 0.45$  (black short dashed line).

684 The oblate particle close to the obstacles flips along the major  
685 axis, contributing to the higher value of diffusivity. We observe  
686 the dynamics deviating away from being sub-diffusive and entering  
687 the super-diffusive phase. The rotational mean-square-displacement  
688 ( $MSD_R$ )<sup>67</sup> is shown in Fig. 14(c), where we observe a shift from the  
689 short time super-diffusive to long time sub-diffusive regime. As for  
690  $MSD_R$ , only the rotating particle contributes because all the other  
691 particles are in the nematic phase and hence show a sub-diffusive  
692 behavior [see Fig. 14(c), red dashed line]. To show that this is a  
693 local effect, we have calculated the orientational self-correlation  $L_2$   
694 as follows:

$$695 L_2(t) = \frac{1}{N} \sum_i \frac{1}{2} (3\hat{n}_i(\tau+t) \cdot \hat{n}_i(\tau) - 1), \quad (28)$$

696 where  $n_i(t)$  is the orientation of the  $i$ th particle at time  $t$ . We have  
697 shown the decay of  $L_2$  as a black dashed line in Fig. 14(d) for a system  
698 without obstacle, with nearly the same  $D_R/D_R^p = 0.19$  (at  $\phi = 0.4$ ).  $L_2$   
699 decays to 0 at  $t_{phy} > 20.0$ . In the presence of obstacles where the bulk  
700 is found to be in the nematic phase and shows  $D_R/D_R^p > 0.19$ ,  $L_2$  can  
701 be observed not decaying [colored dashed lines in Fig. 14(d)]. Thus,  
702 globally, the system is in nematic phase, which leads to a decline in  
703 the rotational dynamics. However, in the presence of obstacles, the  
704 particles are flipping locally and contributing to the super-diffusive  
705 behavior. In this way, the system maintains the nematicity despite  
706 few of the particles being out of the arrested rotational dynamics  
707 phase. The reason for the flipping of oblate particles may be the  
708 misalignment of the particles caused by the presence of obstacles  
709 [Fig. 6(a)]. However, in the prolate case, the particle's alignment  
710 enhances and remains parallel to the cylindrical axis [Fig. 6(b)].  
711 Therefore, the rotational dynamics of the prolate particles in the  
712 presence of obstacles remains frozen.

#### 713 IV. CONCLUSION

714 Experimentally, numerous studies have been performed by  
715 confining the particles in various geometries. In almost all these  
716 studies, it has been shown that the shape anisotropy of the parti-  
717 cles enhances the motion of the self-propelled particle. However, in  
718 the passive particle system, dynamics is governed by the structure  
719 of the fluid. The theoretical prediction of diffusivity for the point  
720 particles is modified to incorporate a finite volume particle, which  
721 agrees with our simulation results. However, with the increase in  
722 shape anisotropy, the diffusivity deviates from the proposed theo-  
723 retical prediction. At a finite volume fraction, the dynamics of the  
724 system become dependent upon structural properties. The structural  
725 property of the spheroidal particle as a result of the introduction  
726 of obstacles in the system influences the dynamics. As shown in  
727 the case of oblate particles, the rotational diffusivity couples with  
728 translational diffusivity, resulting in the flipping motion, leading to  
729 a super-diffusivity behavior. In the present study, for a low particle  
730 concentration regime, the translational diffusivity of the anisotropic  
731 particles behaves nearly the same way as the system of spherical par-  
732 ticles. For a single particle as well as for finite  $\phi$ , diffusing in the  
733 cylindrical pores with extreme confinement, the long-time trans-  
734 lational diffusivity behaves like a one-dimensional system, where  
735 diffusivity scales to one by a third of the diffusivity of the bulk  
736 system.

In the presence of obstacles, the nematic phase has been  
observed to show exciting results. We have shown the nematic direc-  
tor being controlled by the presence of cylindrical obstacles. The  
kinetics of the evolution of the particles' alignment showed that the  
spheroidal particles preferred to align quickly along the axis of the  
cylindrical obstacles. We hope that the present study would help us  
design a system where the nematic alignment can be controlled by  
the surface effects of the obstacles.

#### ACKNOWLEDGMENTS

V.A.V. acknowledges CSIR-UGC and the institute for funding  
this research.

#### AUTHOR DECLARATIONS

##### Conflict of Interest

The authors have no conflicts to disclose.

##### Author Contributions

**Vikki Anand Varma:** Conceptualization (equal); Data curation (lead); Formal analysis (equal); Funding acquisition (lead); Investigation (equal); Methodology (equal); Project administration (supporting); Resources (supporting); Supervision (supporting); Validation (equal); Visualization (equal); Writing – original draft (equal); Writing – review & editing (equal). **Sujin B. Babu:** Conceptualization (lead); Data curation (supporting); Formal analysis (lead); Funding acquisition (supporting); Investigation (lead); Methodology (lead); Project administration (lead); Resources (lead); Supervision (lead); Validation (lead); Writing – original draft (equal); Writing – review & editing (equal).

#### DATA AVAILABILITY

The data that support the findings of this study are available  
from the corresponding author upon reasonable request.

#### REFERENCES

- <sup>1</sup>D. Gomez and S. Klumpp, *Phys. Chem. Chem. Phys.* **18**, 11184 (2016).
- <sup>2</sup>D. S. Banks and C. Fradin, *Biophys. J.* **89**, 2960 (2005).
- <sup>3</sup>M. Zarif and R. K. Bowles, *Phys. Rev. E* **101**, 012908 (2020).
- <sup>4</sup>T. S. Domingues, R. R. Coifman, and A. Haji-Akbari, *J. Phys. Chem. B* **127**, 5273 (2023).
- <sup>5</sup>T. Motegi, H. Nabika, and K. Murakoshi, *Phys. Chem. Chem. Phys.* **15**, 12895 (2013).
- <sup>6</sup>T. Sentjabrskaja, E. Zaccarelli, C. De Michele, F. Sciortino, P. Tartaglia, T. Voigtmann, S. U. Egelhaaf, and M. Laurati, *Nat. Commun.* **7**, 11133 (2016).
- <sup>7</sup>H. W. Cho, G. Kwon, B. J. Sung, and A. Yethiraj, *Phys. Rev. Lett.* **109**, 155901 (2012).
- <sup>8</sup>S. Lifson and J. L. Jackson, *J. Chem. Phys.* **36**, 2410 (1962).
- <sup>9</sup>M. Jardat, B. Hribar-Lee, and V. Vlachy, *Phys. Chem. Chem. Phys.* **10**, 449 (2008).
- <sup>10</sup>P. Illien, O. Bénichou, G. Oshanin, A. Sarracino, and R. Voituriez, *Phys. Rev. Lett.* **120**, 200606 (2018).
- <sup>11</sup>H. Khalilian and H. Fazli, *J. Chem. Phys.* **145**, 164909 (2016).

- 780 <sup>12</sup>D. M. van Roon, G. Volpe, M. M. Telo da Gama, and N. A. M. Araújo, *Soft Matter* **18**, 6899 (2022).  
781  
782 <sup>13</sup>R. Zwanzig, *J. Phys. Chem.* **96**, 3926 (1992).  
783 <sup>14</sup>J. M. Rubí, *Europhys. Lett.* **127**, 10001 (2019).  
784 <sup>15</sup>A. Berezhkovskii and A. Szabo, *J. Chem. Phys.* **135**, 074108 (2011).  
785 <sup>16</sup>T. Bertrand, Y. Zhao, O. Bénichou, J. Tailleur, and R. Voituriez, *Phys. Rev. Lett.* **120**, 198103 (2018).  
786  
787 <sup>17</sup>T. Guérin and D. S. Dean, *Phys. Rev. Lett.* **115**, 020601 (2015).  
788 <sup>18</sup>A. Filippov, H. Soenen, J. Blom, and O. N. Antzutkin, *ACS Omega* **8**, 36534 (2023).  
789  
790 <sup>19</sup>J. Kurzidim, D. Coslovich, and G. Kahl, *Phys. Rev. E* **82**, 041505 (2010).  
791 <sup>20</sup>H. Berry and H. Chaté, *Phys. Rev. E* **89**, 022708 (2014).  
792 <sup>21</sup>M.-B. Luo and D.-Y. Hua, *ACS Omega* **8**, 34188 (2023).  
793  
794 <sup>22</sup>J. M. Sancho, A. M. Lacasta, K. Lindenberg, I. M. Sokolov, and A. H. Romero, *Phys. Rev. Lett.* **92**, 250601 (2004).  
795  
796 <sup>23</sup>H. Hijar, *Phys. Rev. E* **102**, 062705 (2020).  
797  
798 <sup>24</sup>Y. Gu and N. L. Abbott, *Phys. Rev. Lett.* **85**, 4719 (2000).  
799  
800 <sup>25</sup>F. Nakai, M. Kröger, T. Ishida, T. Uneyama, Y. Doi, and Y. Masubuchi, *Phys. Rev. E* **107**, 044604 (2023).  
801  
802 <sup>26</sup>F. van Swol, L. J. Douglas Frink, A. P. Malanoski, and D. N. Petsev, *J. Chem. Phys.* **159**, 084705 (2023).  
803  
804 <sup>27</sup>H.-L. Yeh and J. J. Juárez, *Exp. Therm. Fluid Sci.* **121**, 110282 (2021).  
805  
806 <sup>28</sup>W. P. Krekelberg, V. K. Shen, J. R. Errington, and T. M. Truskett, *J. Chem. Phys.* **135**, 154502 (2011).  
807  
808 <sup>29</sup>F. Zhou, H. Wang, and Z. Zhang, *Langmuir* **36**, 11866 (2020).  
809  
810 <sup>30</sup>M. Brun-Cosme-Bruny, E. Bertin, B. Coasne, P. Peyla, and S. Rafaï, *J. Chem. Phys.* **150**, 104901 (2019).  
811  
812 <sup>31</sup>T. Guérin, N. Levernier, O. Bénichou, and R. Voituriez, *Nature* **534**, 356 (2016).  
813  
814 <sup>32</sup>L. Dai, D. R. Tree, J. R. C. van der Maarel, K. D. Dorfman, and P. S. Doyle, *Phys. Rev. Lett.* **110**, 168105 (2013).  
815  
816 <sup>33</sup>M. J. Simpson and M. J. Plank, *Results Phys.* **7**, 3346 (2017).  
817  
818 <sup>34</sup>Y. Farah, D. Loghin, A. Tzella, and J. Vanneste, *Proc. R. Soc. A* **476**, 20200072 (2020).  
819  
820 <sup>35</sup>M. Mangeat, T. Guérin, and D. S. Dean, *J. Chem. Phys.* **152**, 234109 (2020).  
821  
822 <sup>36</sup>A. J. Ellery, R. E. Baker, and M. J. Simpson, *Phys. Biol.* **12**, 066010 (2015).  
823  
824 <sup>37</sup>L. Dagdug, M.-V. Vazquez, A. M. Berezhkovskii, V. Y. Zitserman, and S. M. Bezrukov, *J. Chem. Phys.* **136**, 204106 (2012).  
825  
826 <sup>38</sup>S. K. Ghosh, A. G. Cherstvy, and R. Metzler, *Phys. Chem. Chem. Phys.* **17**, 1847 (2015).  
827  
828 <sup>39</sup>V. A. Varma, I. Malhotra, and S. B. Babu, *Phys. Rev. E* **106**, 014602 (2022).  
829  
830 <sup>40</sup>A. Poniewierski and R. Holyst, *Phys. Rev. A* **38**, 3721 (1988).  
831  
832 <sup>41</sup>T. Khatun, M. D. Choudhury, T. Dutta, and S. Tarafdar, *Phys. Rev. E* **86**, 016114 (2012).  
833  
834 <sup>42</sup>T. Boeck, H.-A. Bahr, S. Lampenscherf, and U. Bahr, *Phys. Rev. E* **59**, 1408 (1999).  
835  
836 <sup>43</sup>B. Langeslay, W. Fahy, and G. Juarez, *arXiv:2401.17222* (2024).  
837  
838 <sup>44</sup>M. Robert de Saint Vincent, M. Abkarian, and H. Tabuteau, *Soft Matter* **12**, 1041 (2016).  
839  
840 <sup>45</sup>Z. Shireen and S. B. Babu, *J. Chem. Phys.* **147**, 054904 (2017).  
841  
842 <sup>46</sup>Z. Shireen and S. B. Babu, *Soft Matter* **14**, 9271 (2018).  
843  
844 <sup>47</sup>M. Adams, Z. Dogic, S. L. Keller, and S. Fraden, *Nature* **393**, 349 (1998).  
845  
846 <sup>48</sup>S. Varga, A. Galindo, and G. Jackson, *J. Chem. Phys.* **117**, 7207 (2002).  
847  
848 <sup>49</sup>B. Senyuk, C. Meng, and I. I. Smalyukh, *Langmuir* **38**, 9099 (2022).  
849  
850 <sup>50</sup>J. W. Perram, J. Rasmussen, E. Praestgaard, and J. L. Lebowitz, *Phys. Rev. E* **54**, 6565 (1996).  
851  
852 <sup>51</sup>S. Babu, J. C. Gimel, and T. Nicolai, *J. Chem. Phys.* **125**, 184512 (2006).  
853  
854 <sup>52</sup>Z. Shireen, T. Curk, C. Brandl, and S. B. Babu, *ACS Omega* **8**, 37225 (2023).  
855  
856 <sup>53</sup>I. Malhotra and S. B. Babu, *J. Chem. Phys.* **151**, 084901 (2019).  
857  
858 <sup>54</sup>M. Yadav, V. A. Varma, and S. B. Babu, *J. Mol. Liq.* **399**, 124404 (2024).  
859  
860 <sup>55</sup>V. A. Varma, Kritika, J. Singh, and S. B. Babu, *Adv. Theory Simul.* **■**, 2200666 (2023).  
861  
862 <sup>56</sup>V. A. Varma, S. Jaglan, M. Y. Khan, and S. B. Babu, *Phys. Chem. Chem. Phys.* **26**, 1385 (2024).  
863  
864 <sup>57</sup>A. Poniewierski, R. Holyst, *Phys. Rev. A* **38**, 3721 (1988).  
865  
866 <sup>58</sup>D. Medlin and G. Snyder, *Curr. Opin. Colloid Interface Sci.* **14**, 226 (2009).  
867  
868 <sup>59</sup>K. H. Kil, A. Yethiraj, and J. S. Kim, *Phys. Rev. E* **101**, 032705 (2020).  
869  
870 <sup>60</sup>S. Babu, J.-C. Gimel, T. Nicolai, and C. De Michele, *J. Chem. Phys.* **128**, 204504 (2008).  
871  
872 <sup>61</sup>C. De Michele, R. Schilling, and F. Sciortino, *Phys. Rev. Lett.* **98**, 265702 (2007).  
873  
874 <sup>62</sup>G. Goel, W. P. Krekelberg, M. J. Pond, J. Mittal, V. K. Shen, J. R. Errington, and T. M. Truskett, *J. Stat. Mech.: Theory Exp.* **2009**, P04006.  
875  
876 <sup>63</sup>I. C. Kim and S. Torquato, *J. Chem. Phys.* **96**, 1498 (1992).  
877  
878 <sup>64</sup>J. Machta and R. Zwanzig, *Phys. Rev. Lett.* **50**, 1959 (1983).  
879  
880 <sup>65</sup>D. Reguera and J. M. Rubí, *Phys. Rev. E* **64**, 061106 (2001).  
881  
882 <sup>66</sup>S. Babu, J. C. Gimel, and T. Nicolai, *J. Phys. Chem. B* **112**, 743 (2008).  
883  
884 <sup>67</sup>K. V. Edmond, M. T. Elsesser, G. L. Hunter, D. J. Pine, and E. R. Weeks, *Proc. Natl. Acad. Sci. U. S. A.* **109**, 17891 (2012).  
885  
886